Check for updates

Advanced Materials Interfaces

ADVANCED MATERIALS INTERFACES Open Access

www.advmatinterfaces.de

RESEARCH ARTICLE OPEN ACCESS

Redox-Confined Interfacial Polymerization Enables Mechanically Robust and Self-Adhesive Nanofilms

Luana Gazzato[1] | Vivek Manish[2] | Giorgio Speranza[3,4,5] | Maria F. Pantano[2] | Marco Frasconi[1]

[1]Department of Chemical Sciences, University of Padova, Padova, Italy | [2]Department of Civil, Environmental and Mechanical Engineering, University of Trento, Trento, Italy | [3]Center for Sensors and Devices, Fondazione Bruno Kessler, Trento, Italy | [4]Istituto Di Fotonica e Nanotecnologie, Consiglio Nazionale Delle Ricerche IFN-CNR, Trento, Italy | [5]Department of Industrial Engineering, University of Trento, Trento, Italy

Correspondence: Maria F. Pantano (maria.pantano@unitn.it) | Marco Frasconi (marco.frasconi@unipd.it)

Received: 20 April 2026 | **Revised:** 13 July 2026 | **Accepted:** 25 July 2026

Keywords: adaptive materials | biointerfaces | freestanding membranes | nanomechanics | wearable devices

ABSTRACT

Robust polymer nanofilms are increasingly important for applications that require mechanically strong yet compliant membranes with nanoscale thickness and intimate interfacial contact. While biological membranes naturally combine flexibility, adaptability, and adhesion, achieving these features in synthetic nanomembranes remains challenging. Here, we report a one-step strategy for the synthesis of centimeter-scale, freestanding nanofilms via redox-confined interfacial polymerization at a liquid-liquid interface. Oxidative coupling of a multifunctional thiol monomer is spatially restricted to the aqueous-organic interface, yielding continuous membranes with precisely tunable thicknesses ranging from tens to hundreds of nanometers. Structural and surface analyses reveal uniform network formation across all film thicknesses, consistent with a diffusion-controlled growth mechanism. The resulting nanofilms exhibit high Young's modulus (425 MPa) and tensile strength (38 MPa), solid-like viscoelastic behavior, and intrinsic adhesion to artificial skin despite the absence of dedicated bioadhesive functionalization. Together, these results establish redox-confined interfacial polymerization as a versatile fabrication route to mechanically robust, freestanding nanomembranes with potential relevance for wearable sensing platforms, therapeutic interfaces, separation membranes, and other applications requiring strong ultrathin films with intrinsic adhesion.

1 | Introduction

Polymer films with nanoscale thickness are attracting growing interest for applications spanning flexible electronics [1, 2], energy storage [3, 4], and biomedical interfaces [5–7]. Reducing film thickness to the nanoscale offers unique advantages, including improved compliance with human skin for medical diagnostics and human–machine interactions [8], as well as enhanced permeability for molecular separation [9, 10], thereby motivating intensive efforts toward the fabrication of polymeric nanofilms. However, although numerous methods exist for depositing thin polymer layers on solid substrates, simple and general methods to fabricate large-area, freestanding nanomembranes that are mechanically robust, chemically well-defined, and substrate-independent remain limited [11, 12], particularly when avoiding multistep processing. Conventional approaches for producing freestanding polymer nanofilms typically involve thin-film deposition onto solid substrates, such as spin coating, followed by sacrificial-layer release [13]. Although effective and widely used, these methods rely on substrate support during fabrication and require sequential processing steps, including film release and transfer. Alternative interfacial assembly strategies, such as layer-by-layer assembly [14] and Langmuir-Blodgett deposition [15], enable precise control over nanoscale thickness; however, they often depend on specific molecular design constraints, including amphiphilicity or tailored surface activity. Interfacial synthesis

This is an open access article under the terms of the Creative Commons Attribution License, which permits use, distribution and reproduction in any medium, provided the original work is properly cited.

© 2026 The Author(s). *Advanced Materials Interfaces* published by Wiley-VCH GmbH

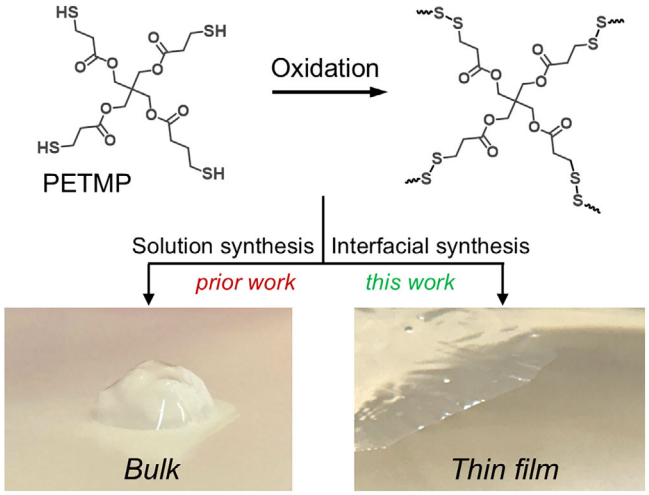


FIGURE 1 | Synthesis of disulfide-crosslinked materials by oxidation reaction of thiols from PETMP. This monomer was previously used to prepare bulk polymers. Interfacial synthesis at the liquid-liquid interface provides ultra-thin films with remarkable mechanical properties.

at liquid–liquid or liquid–air interfaces offers a powerful route to control polymerization within a confined geometry, yielding films with nanometer thickness [16]. Ideally, the fabricated membranes should be able to combine flexibility and durability in order to withstand mechanical stresses without compromising performance or structural integrity. This is not a simple target to achieve, especially with conventional polymers, where irreversible bond formation often leads to defects in growing films with no means of error correction. To address this limitation, dynamic covalent chemistry has emerged as a powerful strategy, combining the robustness of covalent bonding with reversible bond exchange. Dynamic covalent linkages, such as boronate esters (B—O) [17] and imines (C—N) [18], have been exploited to fabricate polymeric films. In this context, disulfide-mediated polymerization is particularly appealing. Disulfide bonds (S—S), ubiquitous in proteins, impart reversible stability and adaptive behavior in biological systems [19] and endow synthetic polymers with biocompatibility [20] and recyclability [21]. Their ability to break and reform under mild redox conditions further broadens their functionality, enabling materials that couple responsiveness with mechanical durability [22, 23] and adhesive properties [24]. However, despite their widespread use in bulk polymers and gels, translating these advantages into thin, continuous films remains challenging, largely due to poor control over disulfide crosslinking at the nanoscale, ultimately constraining reliable film fabrication.

Here, we report the one-step fabrication of freestanding, mechanically robust disulfide-crosslinked films with precisely tunable nanoscale thickness, driven by oxidative coupling of multifunctional thiol monomers at the interface between two immiscible liquids (Figure 1). The films form in situ from pentaerythritol tetrakis(3-mercaptopropionate) (PETMP), a widely used monomer, in the presence of triethylamine (TEA) and hydrogen peroxide (H_2O_2). This confined interfacial reaction enables precise control over crosslinking without the need for amphiphilic precursors or complex templates. The resulting disulfide-crosslinked nanofilms exhibit high Young's modulus, tensile strength, and adhesion to artificial skin, the latter highlighting their mechanical compliance with soft interfaces. This combination of properties at the nanoscale makes these films an attractive platform for the development of wearable sensors and therapeutic interfaces.

2 | Results and Discussion

Figure 2a illustrates the formation of disulfide-crosslinked nanofilms at the interface between a toluene phase containing the PETMP monomer and an aqueous phase containing TEA and H_2O_2. At this toluene-water boundary, TEA deprotonates PETMP to generate reactive thiolate species, which are subsequently oxidized by H_2O_2 to form disulfide linkages. This spatial separation of the monomer and oxidant drives a confined interfacial polymerization, resulting in the formation of a continuous crosslinked film. After polymerization, the film was transferred from the interface and floated on the water surface, allowing the removal of residual reagents. Figure 2b shows a PETMP-crosslinked nanofilm about 250 nm in thickness and 5 cm in diameter, obtained after a 72 h reaction, floating on a water surface. By increasing the reactor diameter while maintaining the same reaction conditions, continuous freestanding nanofilms with diameters up to 10 cm were readily obtained (Figure S1), demonstrating the scalability of the fabrication strategy. Notably, despite its large lateral dimensions, the film remains intact and free of visible defects. The floated film exhibited remarkable mechanical robustness, as pressing it with thin-tipped tweezers resulted in only elastic bending without visible damage (Figure 2c and Figure S2). The films can be readily transferred onto various substrates, such as glass, silica, quartz, or collected as freestanding membranes. Once transferred onto a paper frame and dried, the freely suspended nanofilms remained intact, transparent, and free of visible defects over areas of several square centimeters (Figure 2d). They also displayed excellent flexibility, maintaining their structural integrity even under repeated bending. Optical measurements revealed a high transmittance exceeding 95% across the 400–800 nm range (Figure S3), consistent with their smooth surface morphology.

To further demonstrate their robustness, a dried nanofilm was self-adhered to the end of a plastic tube (1.5 cm in diameter) and was able to support a 4 mL column of liquid without rupturing (Figure 2e). The weight of the contained liquid was approximately 70 000 times greater than that of the freestanding portion of the nanofilm, distributed over a centimeter-scale area, highlighting an exceptional load-to-weight ratio. During the test, the film visibly deformed as the liquid accumulated, evidencing its flexibility, while the absence of any leakage confirmed its water impermeability and strong adhesion to the plastic tube.

To optimize film synthesis and gain further insight into the formation process, nanofilms obtained at different reaction times were transferred from the reactor to silicon substrates and characterized using atomic force microscopy (AFM). After 6 h of reaction, a continuous film with a thickness of 25 nm and a root-mean-square (RMS) roughness of approximately 1 nm was obtained (Figure 3a,b). The film thickness increased progressively with reaction time, reaching 75 nm at 12 h, 96 nm at 24 h, 129 nm at 48 h, 250 nm at 72 h, 418 nm at 96 h, and 434 nm at 120 h (Figure 3c

21967350, 2026, 18, Downloaded from https://advanced.onlinelibrary.wiley.com/doi/10.1002/admi.70632 by Maria Pantano - Universita Di Trento , Wiley Online Library on [13/10/2026]. See the Terms and Conditions (https://onlinelibrary.wiley.com/terms-and-conditions) on Wiley Online Library for rules of use; OA articles are governed by the applicable Creative Commons License

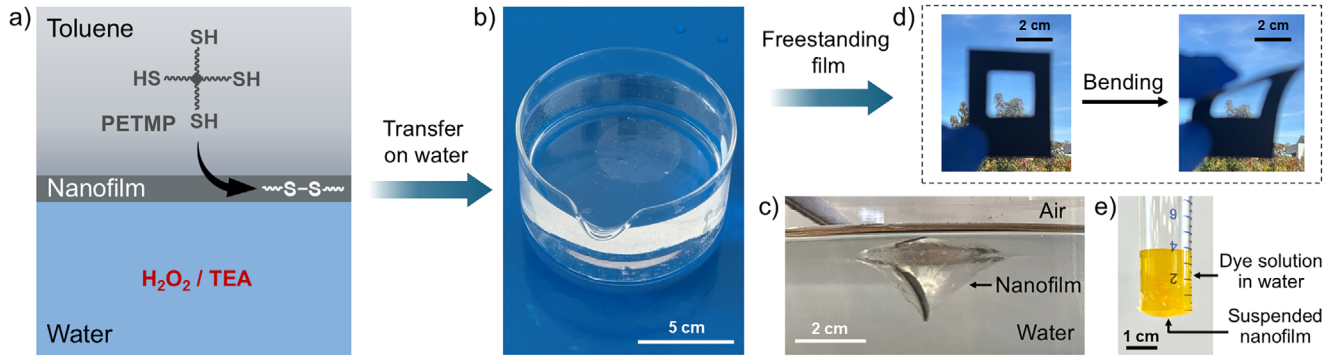


FIGURE 2 | (a) Schematic of the synthesis of the disulfide-crosslinked nanofilms by oxidation reaction of thiols at the toluene-water interface. The film forms at the interface between the aqueous phase, containing H_2O_2 and TEA, and the toluene phase containing the PETMP monomer. (b) Photograph of a nanofilm (5 cm in diameter) transferred from the reaction interface and refloated on a water surface. (c) Demonstration of the robustness of a floating nanofilm under poking and pressing with tweezers. (d) Freestanding nanofilm suspended on a paper frame, highlighting its mechanical flexibility and optical transparency. (e) Nanofilm self-adhered to the end of a plastic tube, supporting a column of water (colored with dye) without leakage.

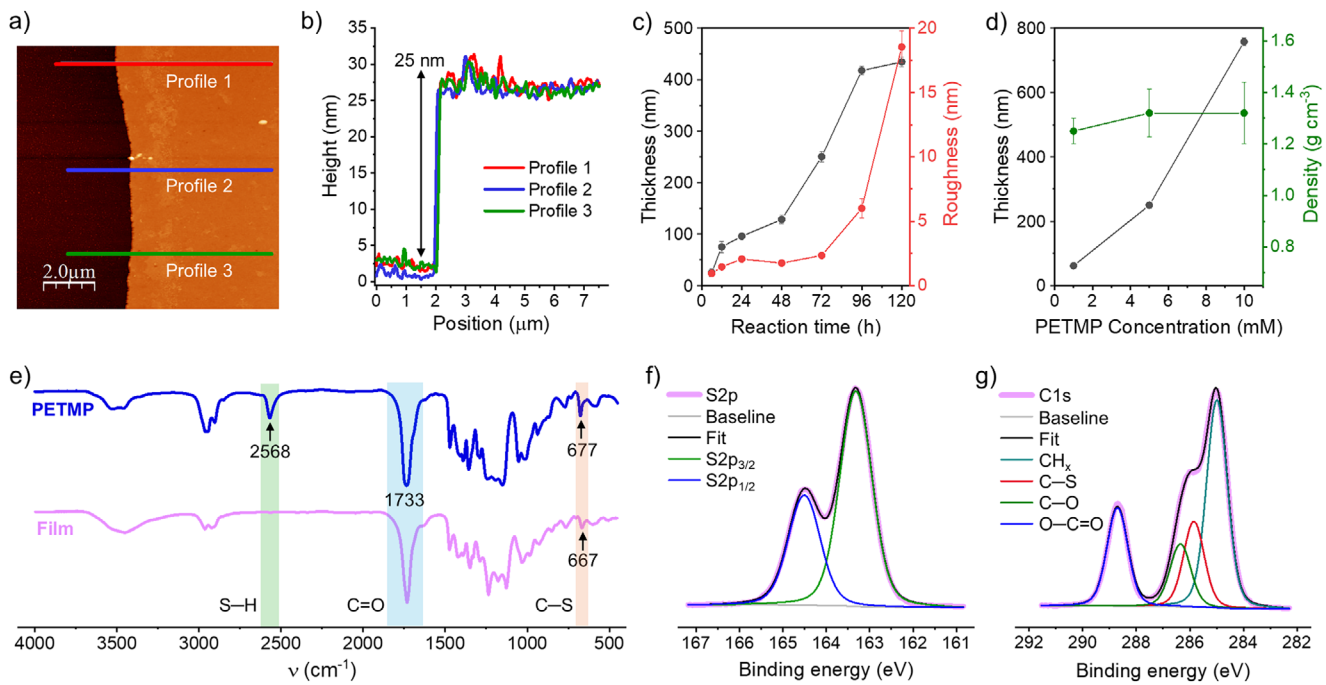


FIGURE 3 | (a) Tapping-mode AFM height image and (b) corresponding thickness profile of a disulfide-crosslinked nanofilm transferred onto a silicon substrate. The film was prepared using 5 mM PETMP and 10 mM H_2O_2/TEA for 6 h. (c) Variation of film thickness and root-mean-square (RMS) roughness, evaluated by AFM, as a function of reaction time (5 mM PETMP and 10 mM H_2O_2/TEA). (d) Dependence of film thickness and density on PETMP concentration (10 mM H_2O_2/TEA, 72 h reaction). (e) FT-IR spectra of the PETMP monomer and nanofilm. f) XPS S 2p and (g) C 1s narrow-scan spectra of the nanofilm.

and Figure S4). In all cases, the film surfaces remained compact and free of pinholes, although a significant number of particulates were observed on the film for reaction times longer than 72 h. The mass density, calculated from the mass of the films measured by quartz crystal microbalance (QCM) after transferring the samples onto gold-coated QCM crystals, remained constant across all reaction times, ranging from 1.36 to 1.41 g cm^{-3} (Table S1). These values are consistent with those previously reported for polyamide nanofilms measured by QCM, typically in the range of 1.22–1.44 g cm^{-3} [25]. The water contact angles of the nanofilms obtained at different reaction times ranged from 65° to 70°, indicating comparable surface polarity across all samples. This consistency in both density and wettability suggests uniform disulfide crosslinking and surface composition throughout film growth. The influence of the temperature on film growth was also investigated under the optimized reaction conditions. Performing interfacial polymerization at 4°C for 72 h produced thinner nanofilms (172 nm) with higher surface roughness compared to those synthesized at room temperature (Figure S5 and Table S1), indicating that lowering the temperature slows the interfacial

21967350, 2026, 18, Downloaded from https://advanced.onlinelibrary.wiley.com/doi/10.1002/admi.70632 by Maria Pantano - Universita Di Trento , Wiley Online Library on [13/10/2026]. See the Terms and Conditions (https://onlinelibrary.wiley.com/terms-and-conditions) on Wiley Online Library for rules of use; OA articles are governed by the applicable Creative Commons License

polymerization process. In contrast, no significant differences were observed in the film density or water contact angle, suggesting that temperature primarily affects the polymerization kinetics rather than the packing of the resulting disulfide-crosslinked nanofilms.

The quality of the nanofilms was strongly influenced by the concentrations of PETMP, TEA, and H_2O_2. Systematic variation of these parameters revealed that optimal conditions were obtained using 5 mM PETMP in toluene and equimolar concentrations (10 mM) of TEA and H_2O_2 in water. Increasing the PETMP concentration from 1 to 10 mM resulted in a gradual increase in film thickness from 62 to 758 nm (Figure 3d and Figure S6), indicating that thickness can be precisely tuned by adjusting the initial monomer concentration. At a low PETMP concentration (1 mM), the films exhibited surface defects, including holes, increased roughness (~5.6 nm), and a slightly lower density (1.26 g cm^{-3}). In contrast, higher PETMP concentrations promoted faster polymerization, yielding smooth, continuous films. The influence of TEA concentration on nanofilm formation was also investigated while maintaining the H_2O_2 concentration constant (Figure S7 and Table S1). Increasing the TEA concentration from 1 to 100 mM progressively increased the film thickness from 18 to 514 nm, indicating that the basicity of the aqueous phase plays a key role in regulating film growth. At the highest TEA concentration, the films exhibited increased surface roughness (approximately 15 nm), likely due to the deposition of polymer aggregates formed during the accelerated interfacial polymerization. In contrast, the film density and water contact angle remained largely unchanged, with only a slight decrease observed at the highest TEA concentration. These results indicate that varying the concentration of TEA primarily influences the growth kinetics while only marginally affecting the packing density and surface properties of the resulting nanofilms. Decreasing the concentrations of H_2O_2 and TEA to 5 mM (with 5 mM PETMP) reduced the film thickness from 250 to 94 nm (Figure S8) and slightly lowered the water contact angle to 60°, likely due to incomplete oxidation of PETMP thiol groups, which produced a more polar surface. As controls, when the aqueous phase contained only TEA or only H_2O_2, no film formation occurred at the interface. The dependence of film thickness on reagent concentrations indicates that the interfacial polymerization is governed by diffusion-controlled redox kinetics, where the steady supply of monomer and oxidant species across the liquid–liquid boundary determines the rate of network growth. Based on these results, subsequent characterizations were conducted using 5 mM PETMP and 10 mM TEA/ H_2O_2 with a reaction time of 72 h, which consistently produced robust and smooth nanofilms.

The chemical composition of the films was characterized by Fourier-transform infrared (FT-IR) spectroscopy, elemental analysis, and x-ray photoelectron spectroscopy (XPS). FTIR spectra provided clear evidence of complete disulfide crosslinking, as the S—H stretching band of the PETMP monomer at 2568 cm^{-1} was no longer detectable in the spectra of the resulting films (Figure 3e and Figure S9), consistent with previous investigations on bulk PETMP-based polymers [26]. In addition, the C—S stretching band shifts from 677 cm^{-1} in the monomer to 667 cm^{-1} in the film, consistent with thiol oxidation and network crosslinking. The persistence of the carbonyl (C═O) stretching band at 1733 cm^{-1} indicates that the PETMP backbone remains intact throughout the polymerization process. Elemental analysis of the films showed good agreement with the theoretical composition and revealed a lower hydrogen content than that of the monomer (Table S2), consistent with the formation of the expected crosslinked disulfide polymer network. The XPS spectrum of the film further confirms the formation of the disulfide crosslinked polymer. The deconvolution of the S 2p region reveals two components at 163.4 and 164.6 eV, corresponding to the S $2p_{3/2}$ and S $2p_{1/2}$ spin–orbit doublet of sulfur atoms in the C—S environment (Figure 3f). The C 1s spectrum exhibits four components assigned to C—C/C—H (285.0 eV), C—S (286.0 eV), C—O (286.6 eV), and C═O/O—C═O (288.8 eV), which, together with the components observed in the O 1s spectrum (Figure S9), confirm the expected functionalities of the PETMP framework.

We next investigated the mechanical properties of the nanofilms to assess their suitability for applications requiring robust, freestanding materials. The mechanical characterization was performed on films prepared under the optimized conditions (5 mM PETMP in toluene, 10 mM TEA/H_2O_2 in water, 72 h), which yield smooth, continuous freestanding membranes suitable for tensile testing over millimeter-scale spans. Films grown at extended times (>72 h) exhibit increased surface roughness and were therefore not considered for mechanical testing. Owing to their nanoscale thickness, tensile tests were performed using a custom-made platform [27]. This testing device was previously validated [27] and applied to perform tensile tests on PMMA nanomembranes (180–280 nm thick) [28] and on covalent organic framework films with thicknesses below 100 nm and areas of 0.3–0.5 mm^2 [29, 30], demonstrating its reliability for ultrathin freestanding films. To enable tensile testing of the disulfide nanofilms over a large freestanding area, relevant to many thin-film device applications, the film was transferred onto a pre-notched silicon substrate featuring two adjacent support pads (Figure 4a,b), creating a freestanding span of approximately 1 mm (gauge length), while the remaining areas of the film specimen remained in contact with the underlying silicon (Figure S10). This configuration defined a freestanding testing area of about 2 mm^2, allowing a more representative assessment of the film's mechanical behavior over large areas relevant to practical applications.[12] Figure 4c shows the stress–strain curves of the disulfide-crosslinked nanofilms. The films exhibited a tensile strength of 38 ± 3 MPa, a failure strain of 16 ± 8%, a Young's modulus of 425 ± 176 MPa, and a toughness of 4.1 ± 2.8 MJ m^{-3} (see Table S3). These values reveal a distinct combination of stiffness, load-bearing capacity, and extensibility that is rarely achieved in freestanding nanoscale polymer films.[12] For comparison, tensile tests on 30 nm-thick freestanding polystyrene films reported a Young's modulus of 2.8 ± 0.3 GPa and a maximum stress of 48.7 ± 8.9 MPa, with failure occurring at strains below 2.25% [31]. A 95 nm–thick polydimethylsiloxane (PDMS) film reinforced with polyurethane nanofibers exhibited a Young's modulus of 12.5 ± 2.6 MPa, toughness of 3.4 ± 0.1 MJ m^{-3}, and a maximum stress of about 10 MPa with ~60% strain at maximum stress [6]. With specific reference to disulfide-based systems, bulk PETMP-based gels exhibited Young's moduli roughly three orders of magnitude lower (0.0271–1.745 MPa) while showing comparable or slightly higher breaking strains (13.9–30.8%) [32]. Overall, these comparisons highlight that the disulfide nanofilms developed in this work combine the strength typical of rigid polymer networks with the stretchability of soft materials.

21967350, 2026, 18, Downloaded from https://advanced.onlinelibrary.wiley.com/doi/10.1002/admi.70632 by Maria Pantano - Universita Di Trento , Wiley Online Library on [13/10/2026]. See the Terms and Conditions (https://onlinelibrary.wiley.com/terms-and-conditions) on Wiley Online Library for rules of use; OA articles are governed by the applicable Creative Commons License

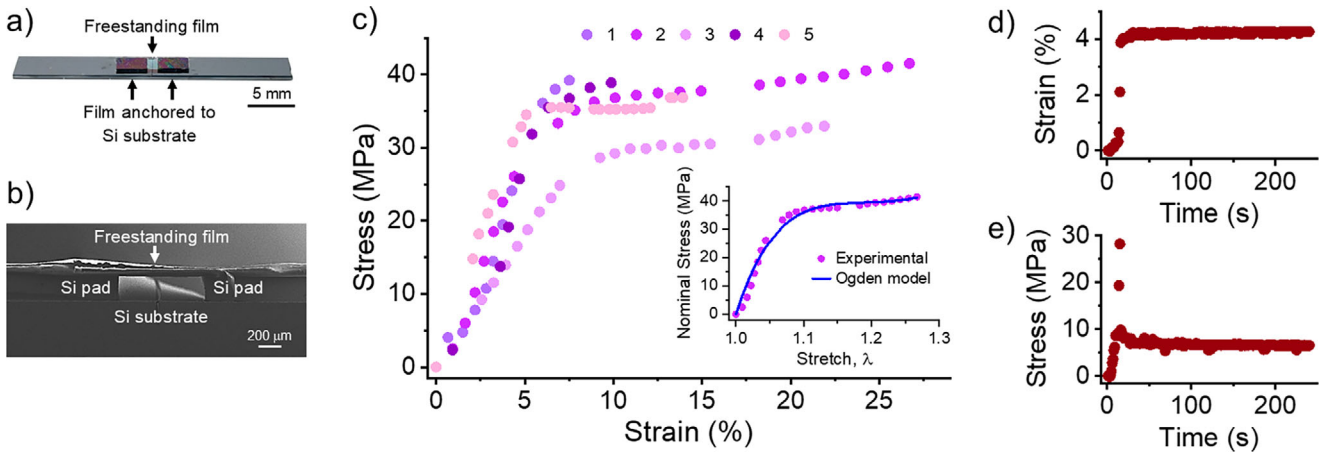


FIGURE 4 | (a) Photograph of a nanofilm specimen transferred onto a silicon substrate for mechanical testing. (b) SEM image showing the nanofilm freely suspended between two silicon pads. (c) Stress–strain curves of nanofilm specimens (five samples tested, each obtained from independent synthesis batches). Inset: stress–stretch response of the disulfide film under monotonic uniaxial loading fitted with the Ogden model. (d,e) Time-dependent mechanical behavior of the disulfide film under constant stretch loading (d) and corresponding stress response (e).

Regarding the mechanical response, all stress–strain curves exhibited a nonlinear regime. To examine this behavior, the initial, intermediate, and final stiffnesses, defined as the local slope of the stress–strain curve [33], were analyzed for a representative sample, yielding values of 274, 25, and 38 MPa, respectively. This evolution reveals a softening-hardening transition, likely arising from network rearrangements within the densely crosslinked disulfide structure. At low strain, reversible network relaxation and local adjustments of the structure lead to temporary softening, whereas at higher deformation, the restricted mobility of the network results in a progressive increase in stiffness before failure. The experimental stress–strain behavior was well described by the Ogden model (Figure 4c, inset), which captures the deformation of isotropic, homogeneous, and incompressible materials under uniaxial tension [34, 35]. The model yielded a shear modulus of ~254 MPa for the disulfide nanofilm. To investigate the time-dependent mechanical behavior, the films were subjected to a constant strain of 4% while monitoring the stress evolution. The resulting response (Figure 4d,e) reveals a solid-like viscoelastic behavior, characterized by an immediate elastic response followed by rapid stress stabilization. This behavior can be attributed to stress redistribution within the densely crosslinked disulfide network, enabling local dissipation of mechanical stress while preserving the integrity of the film during sustained deformation.

The nanofilm's self-adhesiveness, preliminarily demonstrated by its ability to seal a plastic tube, prompted us to quantitatively evaluate its adhesion performance on a skin model using an adhesion separation experiment (Figure 5a). This test was designed to mimic conditions relevant to skin-mounted patches and wearable sensors, where conformal contact and reliable adhesion to soft surfaces are essential [36]. Adhesion energy was quantified as the work of separation per unit area, calculated by integrating the force-displacement response and normalizing by the contact area [37]. For the measurement, a disulfide-crosslinked nanofilm (250 nm thick) was mounted on a plastic frame holder (internal dimensions of 2×2 cm^2). The film was then brought into contact with the skin model under water-wetted conditions over a 1 cm^2 area for 5 min (Figure 5a), after which adhesion force-stroke curves were recorded by lifting the frame with a tensile tester until complete detachment (Figure 5b).

The disulfide-crosslinked nanofilms exhibited a maximum separation force of about 13 ± 2 mN, a separation stroke of 3.5 ± 0.3 mm, and an adhesion energy of 25 ± 4 μJ cm^{-2}. To assess the reliability of our experimental setup, adhesion tests were performed on pristine PDMS nanofilms (346 nm thick). In this case, a maximum separation force of 2.7 ± 0.4 mN, a separation stroke of 4.7 ± 0.9 mm, and an adhesion energy of 6 ± 2 μJ cm^{-2} were obtained (Figure 5c). This latter value is comparable to previously reported adhesion energies for pristine PDMS nanosheets (10.5 μJ cm^{-2}) [37], indicating that the testing methodology provides measurements consistent with the literature. Notably, the disulfide-crosslinked nanofilms exhibit more than four times the adhesion energy measured for the PDMS control under identical conditions, despite being nearly 300 times stiffer in tension than PDMS films (Young's modulus of 1.47 MPa) [37]. The enhanced adhesion of the disulfide-crosslinked nanofilms compared with pristine PDMS can be attributed to the combined effects of their higher surface polarity, ultrathin geometry, and mechanically robust disulfide-crosslinked network. The significantly lower water contact angle of the PETMP-based nanofilms (64–70°) relative to PDMS (109°) promotes stronger polar interactions with the model skin.

To gain further insight into the adhesion mechanism, adhesion experiments were performed under different interfacial conditions. To mimic human sweating conditions, the skin model was wetted with a 0.9 wt.% NaCl solution prior to bringing the nanofilm into contact and performing the adhesion test (Figure S11). Under these conditions, the adhesion energy showed only a slight decrease (19 ± 5 μJ cm^{-2}) compared with that measured on a skin model under water-wetted conditions, indicating that the presence of ions in solution has no significant influence on the adhesion process. This observation is consistent with the nonionic nature of the disulfide-crosslinked nanofilms, suggesting that electrostatic interactions are not a major contributor to adhesion. The adhesion between the nanofilm and the skin model is therefore likely mediated by short-range intermolecular

21967350, 2026, 18, Downloaded from https://advanced.onlinelibrary.wiley.com/doi/10.1002/admi.70632 by Maria Pantano - Universita Di Trento , Wiley Online Library on [13/10/2026]. See the Terms and Conditions (https://onlinelibrary.wiley.com/terms-and-conditions) on Wiley Online Library for rules of use; OA articles are governed by the applicable Creative Commons License

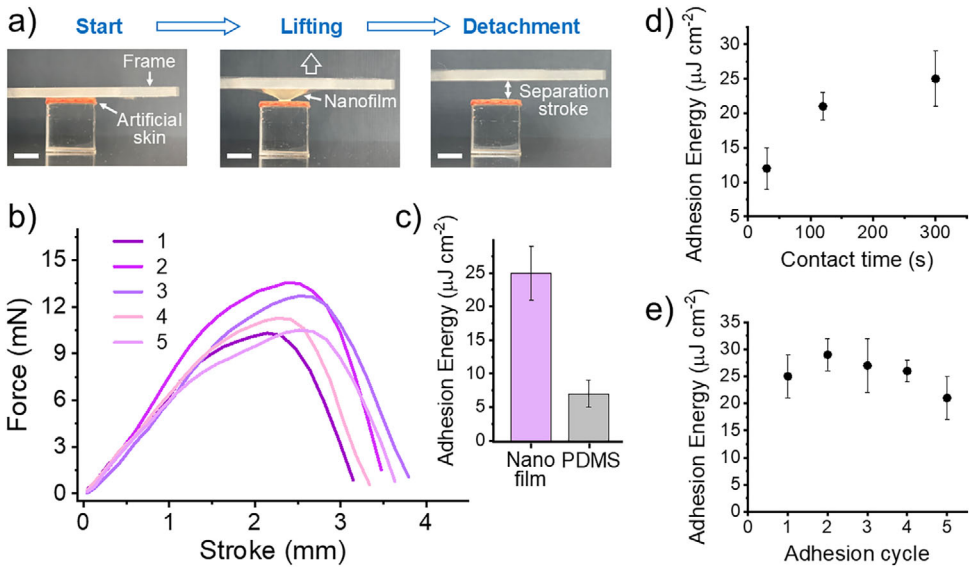


FIGURE 5 | (a) Photographs of the separation process of a disulfide-crosslinked nanofilm, mounted on a plastic frame holder, from artificial skin during the adhesion test (scale bar: 5 mm). (b) Force–stroke curves of disulfide-crosslinked nanofilms (250 nm thick) on artificial skin. Five nanofilm samples were tested, each from an independent synthesis batch. (c) Comparison of the adhesion energy of the disulfide-crosslinked nanofilm and PDMS films on artificial skin. (d) Adhesion energy of nanofilms as a function of the contact time with the artificial skin prior to detachment. (e) Adhesion energy of disulfide-crosslinked nanofilms over repeated adhesion–detachment cycles. All adhesion tests were performed under water-wetted conditions.

interactions, such as van der Waals interactions and hydrogen bonding.

The influence of the contact time between the nanofilm and the skin model prior to the adhesion separation test was also investigated. The adhesion energy approximately doubled as the contact time increased from 30 s to 2 min, whereas extending the contact time to 5 min produced no further increase (Figure 5d). These results indicate that adhesion develops rapidly upon contact and reaches a plateau within a few minutes, consistent with the progressive establishment of intimate conformal contact between the ultrathin nanofilm and the substrate. This mechanical contribution increases the effective interfacial contact area, thereby maximizing the non-covalent intermolecular interactions responsible for adhesion. Finally, the stability of the nanofilm was evaluated through cyclic attachment-detachment tests, in which the nanofilm was repeatedly brought into contact with the skin model for 5 min and subsequently detached using the adhesion separation test. The adhesion energy remained stable over five consecutive adhesion-detachment cycles (Figure 5e), demonstrating that the nanofilms retain their performance during repeated use and suggesting that the disulfide-crosslinked network remains stable under the experimental conditions employed.

When compared with state-of-the-art engineered adhesive nanosheets, our disulfide-crosslinked nanofilms occupy a distinct mechanical-adhesive regime. Polydopamine-modified PDMS films (650 nm thick) [37] reach adhesion energies of 50.7 μJ cm^{-2} and maximum separation forces of 16.6 ± 1.2 mN. Their strong adhesion arises from the combination of soft elastomeric mechanics (Young's moduli in the 10–15 MPa range) and dedicated hydrogen-bonding functionalities such as catechol groups. Remarkably, despite the absence of specific bioadhesive functionalization, our disulfide-crosslinked polymer nanofilms achieve adhesion forces and separation strokes comparable to those of polydopamine–PDMS nanosheets. This behavior is consistent with recent findings showing that an increase of in-plane stiffness in ultrathin films can enhance adhesion by localizing deformation near the detachment front and strengthening interfacial interactions [38, 39]. The adhesion capability demonstrated by our disulfide nanofilms, combined with their mechanical robustness and nanoscale thickness, gives them a unique set of properties not achieved by existing adhesive nanosheets. As such, these films expand the design space for ultrathin polymer membranes that must simultaneously provide load-bearing capacity and conformal adhesion to soft surfaces.

3 | Conclusions

We have demonstrated a straightforward fabrication route for producing freestanding disulfide-crosslinked nanofilms with centimeter-scale areas and precisely tunable thicknesses. The nanofilms are synthesized through oxidative coupling of a readily available thiol monomer at the water-toluene interface, yielding materials that combine high stiffness (Young's modulus of 425 MPa) and toughness. The disulfide network imparts solid-like viscoelasticity, efficient stress redistribution, and strong self-adhesion capable of sealing macroscopic openings and conformally adhering to soft surfaces. These findings highlight redox-confined interfacial polymerization as a versatile strategy for generating mechanically robust ultrathin polymer membranes with integrated adhesive and barrier functionality. Such nanofilms provide a versatile materials platform for flexible, bio-integrated systems, with potential applications spanning sensing devices, therapeutic interfaces, wound-sealing films, and related technologies requiring robust, freestanding ultrathin films. More broadly, this work establishes a redox-driven approach for

21967350, 2026, 18, Downloaded from https://advanced.onlinelibrary.wiley.com/doi/10.1002/admi.70632 by Maria Pantano - Universita Di Trento , Wiley Online Library on [13/10/2026]. See the Terms and Conditions (https://onlinelibrary.wiley.com/terms-and-conditions) on Wiley Online Library for rules of use; OA articles are governed by the applicable Creative Commons License

fabricating polymer nanomembranes under mild, template-free conditions.

4 | Experimental Section

4.1 | Materials and Reagents

All reagents were purchased from commercial suppliers and used without further purification. Pentaerythritol tetrakis(3-mercaptopropionate) (PETMP, >95%), hydrogen peroxide (H_2O_2, 30%), and triethylamine (TEA) were all purchased from Sigma–Aldrich Co (St. Louis, MO). PDMS films were prepared following established procedures reported in the literature [6].

4.2 | Instrumentation

4.2.1 | Atomic Force Microscopy

Atomic force microscopy (AFM) images were taken using an Agilent 5500 Atomic Force Microscope system operating in tapping mode.

4.2.2 | Scanning Electron Microscopy

Scanning electron microscopy (SEM) images were taken on a Zeiss Sigma HD microscope, equipped with a Schottky FEG source, one detector for backscattered electrons and two detectors for secondary electrons (InLens and Everhart Thornley).

4.2.3 | X-Ray Photoemission Spectroscopy

X-ray Photoelectron Spectroscopy (XPS) measurements were collected on the dry films using an Axis DLD Ultra instrument (Kratos, Manchester, UK). The analysis was composed of a wide spectrum on binding energies ranging from −5 to 1250 eV using a 160 eV pass-energy range. High-resolution core line spectra were collected by setting the analyzer pass energy at 20 eV with an energy step of 0.05 eV. Charge comparison was applied, tuning the compensation conditions to maximize the peak intensity while minimizing its FWHM. Spectra were aligned on the binding energy scale, taking the hydrocarbon component of the C 1s core line at 285 eV. Care was taken to select the appropriate background subtraction and Gaussian components for peak fitting.

4.2.4 | UV/Vis Absorption Spectroscopy

UV/Vis Absorption spectra were recorded using a Cary 60 Agilent spectrophotometer.

4.2.5 | FT-IR Spectroscopy

Fourier transform infrared spectra (FT-IR) were obtained with an FT-IR Nicolet Nexus 670 spectrometer. All samples were prepared as KBr pellets. 25 scans were collected with a resolution of 2 cm^{-1}.

4.2.6 | Elemental Analysis

Elemental analysis was performed using a Thermo Scientific Flash 2000 analyzer. The carbon, hydrogen, and nitrogen contents were measured for PETMP as a liquid and for the disulfide films in the solid form.

4.2.7 | Quartz Crystal Microbalance

Quartz Crystal Microbalance (QCM) was carried out using a Q-Sense E1. A gold-coated QCM crystal (QCX 301 from Q-Sense AB) was used as the probe. Free-standing nanofilms were transferred onto the quartz crystal and dried under vacuum. The mass of the films was calculated from the change in oscillating frequency [25], and the mass density was calculated using the film thickness measured by AFM.

4.2.8 | Contact Angle Measurement

Water contact angle measurements were conducted with a Drop Shape Analyzer (Krüss, Germany).

4.3 | Methods

4.3.1 | Synthesis of the Nanofilms

An aqueous solution (15 mL) containing hydrogen peroxide (H_2O_2, final concentration: 10 mM) and triethylamine (TEA, final concentration: 10 mM) was poured into a glass reactor (diameter = 5 cm). Subsequently, a toluene solution (4 mL) of pentaerythritol tetrakis(3-mercaptopropionate) (PETMP, final concentration: 4 mM) was carefully layered onto the aqueous phase using a microliter syringe. The reactor was then sealed, and the reaction was allowed to proceed at room temperature for 3 days.

4.3.2 | Transfer of the Films

After polymerization, the reactor was placed inside a larger crystallizing dish, and Milli-Q water was added slowly with a pipette until the film reached the top edge of the reactor. Then, the larger dish was filled with water until its level slightly exceeded that of the reactor, allowing the film to detach and float on the water surface. The floating film was carefully collected onto a glass slide, gently rinsed with methanol and water, and transferred to a second crystallizing dish filled with water. Finally, the film was collected with a suitable substrate, quartz or silicon, for characterization, or onto a supporting frame to obtain a freestanding film.

4.3.3 | Tensile Tests

Tensile tests on the nanofilms were performed using a custom-made tensile testing platform [27]. This platform combined a piezoelectric motor-driven linear stage (AG-LS25 from Newport) with a minimum incremental displacement of 50 nm, and a

21967350, 2026, 18, Downloaded from https://advanced.onlinelibrary.wiley.com/doi/10.1002/admi.70632 by Maria Pantano - Universita Di Trento , Wiley Online Library on [13/10/2026]. See the Terms and Conditions (https://onlinelibrary.wiley.com/terms-and-conditions) on Wiley Online Library for rules of use; OA articles are governed by the applicable Creative Commons License

calibrated spring fabricated from a 1 mm-thick polyvinyl chloride (PVC) sheet. Each nanofilm specimen was mounted on a pre-notched silicon substrate (3 cm in length and 5 mm in width) featuring two square silicon pads that acted as spacers, raising the film above the substrate surface and creating a freestanding region between them (Figure S10). Prior to testing, the silicon substrate was fractured into two facing blocks by gently applying pressure at one edge while secured within a custom-made clamp designed to prevent undesired movement during fracture [27]. Then, each side of the fractured silicon slice was affixed to the linear stage and the spring. The clamp was then released, and the system was positioned under an optical microscope to initiate tensile measurements. In this configuration, the nanofilm (1.9–2.5 mm in width) was anchored at both ends to the silicon pads, forming a freestanding span corresponding to the gauge length (ranging between 700 and 1100 μm). Tests were performed under ambient conditions. The actuator applied a monotonic displacement, inducing motion of the connected silicon block and, consequently, deforming both the nanofilm and the PVC spring. In this configuration, the film and the spring acted as two elastic elements connected in series and therefore experienced the same load. During tensile testing, optical microscope images were recorded to monitor the displacement of the two silicon pads supporting the film, one of which was attached to the actuator and the other to the spring. Quantitative displacement analysis was performed after the test using custom-developed image-processing software written in C that implemented a fast computation of image correlation. The applied force was obtained by multiplying the displacement of the silicon block connected to the PVC spring by the calibrated spring constant. The stress was calculated by dividing the measured force by the specimen's cross-sectional area, determined from the film width and the thickness measured by AFM. The strain was defined as the relative displacement between the two ends of the film normalized by the gauge length. Young's modulus was determined as the slope of the initial linear region of the stress–strain curve, and the toughness was computed as the area under the stress–strain curve.

4.3.4 | Adhesion Test

The film samples floating on water were transferred to a plastic frame (internal dimensions: 2 cm × 2 cm). The films adhered strongly to the frame. The contact area between the film on the holder and the artificial skin was 1×1 cm^2, which corresponds to the dimensions of the skin model. The film was brought into contact with the skin model for 5 min to ensure initial adhesion. Then, the frame was lifted at 10 mm/min until complete separation from the skin, and the force and stroke were recorded by a tensile tester. The adhesion energy per unit area (μJ cm^{-2}) was calculated as the area under the force–stroke curve normalized by the contact area (1 cm^2).

Author Contributions

Maria F. Pantano: conceptualization, funding acquisition, supervision, resources, Writing – review and editing, methodology, validation. **Giorgio Speranza**: methodology, investigation, validation, data curation, writing – review and editing. **Marco Frasconi**: conceptualization, funding acquisition, writing – review and editing, supervision, resources, methodology, validation. **Luana Gazzato**: investigation, methodology, visualization, formal analysis, data curation, writing – original draft. **Vivek Manish**: methodology, investigation, conceptualization, visualization, formal analysis, data curation, writing – original draft, validation.

Acknowledgements

This research was supported by the MICS (Made in Italy—Circular and Sustainable) Extended Partnership and received funding from Next-GenerationEU (Italian PNRR—M4 C2, Invest 1.3—D.D. 1551.11-10-2022, PE00000004). MFP acknowledges financial support from the European Union-Next Generation EU, Mission 4 Component 2-CUP E53D23005260001.

Open access publishing facilitated by Universita degli Studi di Padova, as part of the Wiley - CRUI-CARE agreement.

Conflicts of Interest

The authors declare no conflicts of interest.

Data Availability Statement

The data that support the findings of this study are available from the corresponding author upon request.

References

1. H. C. Wu, S. Nikzad, C. Zhu, et al., "Highly Stretchable Polymer Semiconductor Thin Films With Multi-Modal Energy Dissipation and High Relative Stretchability," *Nature Communications* 14 (2023): 8382, https://doi.org/10.1038/s41467-023-44099-w.

2. F. Greco, A. Zucca, S. Taccola, B. Mazzolai, and V. Mattoli, "Patterned Free-Standing Conductive Nanofilms for Ultraconformable Circuits and Smart Interfaces," *ACS Applied Materials & Interfaces* 5, no. 19 (2013): 9461–9469, https://doi.org/10.1021/am402142c.

3. S. Jin, P. Chen, S. Hong, et al., "Conformal Zwitterionic Polymer Nanofilms and Lithium Batteries," *Science Advances* 11, no. 41 (2025): 4460, https://doi.org/10.1126/SCIADV.ADY4460.

4. L. K. Beagle, Q. Fang, L. D. Tran, et al., "Synthesis and Tailored Properties of Covalent Organic Framework Thin Films and Heterostructures," *Materials Today* 51 (2021): 427–448, https://doi.org/10.1016/j.mattod.2021.08.007.

5. Z. Rao, F. Ershad, Y. S. Guan, et al., "Ultrathin Rubbery Bio-Optoelectronic Stimulators for Untethered Cardiac Stimulation," *Science Advances* 10, no. 49 (2024): 5061, https://doi.org/10.1126/SCIADV.ADQ5061.

6. Y. Wang, S. Lee, H. Wang, et al., "Robust, Self-Adhesive, Reinforced Polymeric Nanofilms Enabling Gas-Permeable Dry Electrodes for Long-Term Application," *Proceedings of the National Academy of Sciences* 118, no. 38 (2021): 2111904118, https://doi.org/10.1073/PNAS.2111904118.

7. T. Fujie, "Development of Free-Standing Polymer Nanosheets for Advanced Medical and Health-Care Applications," *Polymer Journal* 48, no. 7 (2016): 773–780, https://doi.org/10.1038/pj.2016.38.

8. C. Zhao, J. Park, S. E. Root, and Z. Bao, "Skin-Inspired Soft Bioelectronic Materials, Devices and Systems," *Nature Reviews Bioengineering* 2, no. 8 (2024): 671–690, https://doi.org/10.1038/s44222-024-00194-1.

9. Z. Jiang, R. Dong, A. M. Evans, et al., "Aligned Macrocycle Pores in Ultrathin Films for Accurate Molecular Sieving," *Nature* 609, no. 7925 (2022): 58–64, https://doi.org/10.1038/s41586-022-05032-1.

10. X. Liu, W. Lin, K. Bader Al Mohawes, and N. M. Khashab, "Guanidinium-Based Covalent Organic Framework Membranes for Superior Mono- and Divalent Cations Separation," *Small Structures* 6 (2025): 2400496, https://doi.org/10.1002/sstr.202400496.

21967350, 2026, 18, Downloaded from https://advanced.onlinelibrary.wiley.com/doi/10.1002/admi.70632 by Maria Pantano - Universita Di Trento , Wiley Online Library on [13/10/2026]. See the Terms and Conditions (https://onlinelibrary.wiley.com/terms-and-conditions) on Wiley Online Library for rules of use; OA articles are governed by the applicable Creative Commons License

11. M. Quien, C. L. Ritt, S. S. Garimella, et al., "Interferometric Deflection Analysis of Suspended 2D Polyaramid Thin Films," *Small Methods* 10 (2026): 01543, https://doi.org/10.1002/smtd.202501543.

12. E. Missale, M. Frasconi, and M. F. Pantano, "Ultrathin Organic Membranes: Can They Sustain the Quest for Mechanically Robust Device Applications?," *Iscience* 26, no. 2 (2023): 105924, https://doi.org/10.1016/j.isci.2023.105924.

13. J. Moreira, A. C. Vale, and N. M. Alves, "Spin-Coated Freestanding Films for Biomedical Applications," *Journal of Materials Chemistry B* 9, no. 18 (2021): 3778–3799, https://doi.org/10.1039/d1tb00233c.

14. J. J. Richardson, M. Björnmalm, and F. Caruso, "Technology-Driven Layer-by-Layer Assembly of Nanofilms," *Science* 348, no. 6233 (2015): aaa2491, https://doi.org/10.1126/SCIENCE.AAA2491.

15. O. N. Oliveira, L. Caseli, and K. Ariga, "The Past and the Future of Langmuir and Langmuir–Blodgett Films," *Chemical Reviews* 122, no. 6 (2022): 6459–6513, https://doi.org/10.1021/ACS.CHEMREV.1C00754.

16. F. Zhang, J. Fan, and S. Wang, "Interfacial Polymerization: From Chemistry to Functional Materials," *Angewandte Chemie International Edition* 59, no. 49 (2020): 21840–21856, https://doi.org/10.1002/ANIE.201916473.

17. S. Park, Z. Liao, B. Ibarlucea, et al., "Two-Dimensional Boronate Ester Covalent Organic Framework Thin Films With Large Single Crystalline Domains for a Neuromorphic Memory Device," *Angewandte Chemie International Edition* 59, no. 21 (2020): 8218–8224, https://doi.org/10.1002/ANIE.201916595.

18. M. Matsumoto, L. Valentino, G. M. Stiehl, et al., "Lewis-Acid-Catalyzed Interfacial Polymerization of Covalent Organic Framework Films," *Chemistry* 4, no. 2 (2018): 308–317, https://doi.org/10.1016/j.chempr.2017.12.011.

19. D. Fass, "Disulfide Bonding in Protein Biophysics," *Annual Review of Biophysics* 41, no. 1 (2012): 63–79, https://doi.org/10.1146/ANNUREV-BIOPHYS-050511-102321/CITE/REFWORKS.

20. R. Zhang, T. Nie, Y. Fang, H. Huang, and J. Wu, "Poly(disulfide)s: From Synthesis to Drug Delivery," *Biomacromolecules* 23, no. 1 (2021): 1–19, https://doi.org/10.1021/ACS.BIOMAC.1C01210.

21. D. J. Fortman, R. L. Snyder, D. T. Sheppard, and W. R. Dichtel, "Rapidly Reprocessable Cross-Linked Polyhydroxyurethanes Based on Disulfide Exchange," *ACS Macro Letters* 7, no. 10 (2018): 1226–1231, https://doi.org/10.1021/acsmacrolett.8b00667.

22. G. L. Grocke, H. Zhang, S. S. Kopfinger, S. N. Patel, and S. J. Rowan, "Synthesis and Characterization of Redox-Responsive Disulfide Cross-Linked Polymer Particles for Energy Storage Applications," *ACS Macro Letters* 10, no. 12 (2021): 1637–1642, https://doi.org/10.1021/ACSMACROLETT.1C00682.

23. R. Baretta, M. F. Pantano, and M. Frasconi, "Transient Stiffness Patterning in Hydrogels Driven by Dissipative Mechanochemical Coupling," *Advanced Functional Materials* 35, no. 42 (2025): 2502531, https://doi.org/10.1002/adfm.202502531.

24. B. T. Michal, E. J. Spencer, and S. J. Rowan, "Stimuli-Responsive Reversible Two-Level Adhesion From a Structurally Dynamic Shape-Memory Polymer," *ACS Applied Materials & Interfaces* 8, no. 17 (2016): 11041–11049, https://doi.org/10.1021/acsami.6b01251.

25. S. Karan, Z. Jiang, and A. G. Livingston, "Sub–10 nm Polyamide Nanofilms With Ultrafast Solvent Transport for Molecular Separation," *Science* 348, no. 6241 (2015): 1347–1351, https://doi.org/10.1126/SCIENCE.AAA5058.

26. H. A. Patel, M. S. Yavuz, and C. T. Yavuz, "Exceptional Organic Solvent Uptake by Disulfide-Linked Polymeric Networks," *RSC Advances* 4, no. 46 (2014): 24320–24323, https://doi.org/10.1039/c4ra03355h.

27. M. F. Pantano, G. Speranza, C. Galiotis, and N. Pugno, "A Mechanical System for Tensile Testing of Supported Films at the Nanoscale," *Nanotechnology* 29, no. 39 (2018): 395707, https://doi.org/10.1088/1361-6528/aacf50.

28. M. F. Pantano, C. Pavlou, M. G. Pastore Carbone, C. Galiotis, N. M. Pugno, and G. Speranza, "Highly Deformable, Ultrathin Large-Area Poly(Methyl Methacrylate) Films," *ACS Omega* 6, no. 12 (2021): 8308–8312, https://doi.org/10.1021/acsomega.1c00016.

29. L. Gazzato, E. Missale, D. Asnicar, et al., "Structural Insights Into the Mechanical Behavior of Large-Area 2D Covalent Organic Framework Nanofilms," *ACS Applied Materials & Interfaces* 17, no. 17 (2025): 25819–25827, https://doi.org/10.1021/acsami.5c03512.

30. M. F. Pantano, E. Missale, L. Gazzato, et al., "Large Freestanding 2D Covalent Organic Framework Nano Films Exhibiting High Strength and Stiffness," *Materials Today Chemistry* 26 (2022): 101007, https://doi.org/10.1016/j.mtchem.2022.101007.

31. R. K. Bay and A. J. Crosby, "Uniaxial Extension of Ultrathin Freestanding Polymer Films," *ACS Macro Letters* 8, no. 9 (2019): 1080–1085, https://doi.org/10.1021/acsmacrolett.9b00408.

32. N. Naga, K. Moriyama, and H. Furukawa, "Synthesis and Properties of Multifunctional Thiol Crosslinked Gels Containing Disulfide Bond in the Network Structure," *Journal of Polymer Science Part A: Polymer Chemistry* 55, no. 22 (2017): 3749–3756, https://doi.org/10.1002/POLA.28760.

33. V. Manish, A. Arockiarajan, and G. Tamadapu, "Influence of Water Content on the Mechanical Behavior of Gelatin Based Hydrogels: Synthesis, Characterization, and Modeling," *International Journal of Solids and Structures* 233 (2021): 111219, https://doi.org/10.1016/J.IJSOLSTR.2021.111219.

34. M. J. Lohr, G. P. Sugerman, S. Kakaletsis, E. Lejeune, and M. K. Rausch, "An Introduction to the Ogden Model in Biomechanics: Benefits, Implementation Tools and Limitations," *Philosophical Transactions of the Royal Society A: Mathematical, Physical and Engineering Sciences* 380, no. 2234 (2022): 20210365, https://doi.org/10.1098/RSTA.2021.0365/112293.

35. R. W. Ogden, "Large Deformation Isotropic Elasticity—on the Correlation of Theory and Experiment for Incompressible Rubberlike Solids," *Proceedings of the Royal Society of London A Mathematical and Physical Sciences* 326, no. 1972 (1567): 565–584, https://doi.org/10.1098/rspa.1972.0026.

36. S. J. Wu and X. Zhao, "Bioadhesive Technology Platforms," *Chemical Reviews* 123, no. 24 (2023): 14084–14118, https://doi.org/10.1021/ACS.CHEMREV.3C00380.

37. K. Yamagishi, I. Kirino, I. Takahashi, et al., "Tissue-Adhesive Wirelessly Powered Optoelectronic Device for Metronomic Photodynamic Cancer Therapy," *Nature Biomedical Engineering* 3, no. 1 (2018): 27–36, https://doi.org/10.1038/s41551-018-0261-7.

38. C. Yu, W. Zeng, B. Wang, et al., "Stiffer Is Stickier: Adhesion in Elastic Nanofilms," *Nano Letters* 25, no. 5 (2025): 1876–1882, https://doi.org/10.1021/ACS.NANOLETT.

39. Z. Fang, Z. Dai, B. Wang, et al., "Pull-to-Peel of Two-Dimensional Materials for the Simultaneous Determination of Elasticity and Adhesion," *Nano Letters* 23, no. 2 (2023): 742–749, https://doi.org/10.1021/ACS.NANOLETT.

Supporting Information

Additional supporting information can be found online in the Supporting Information section.

Supporting File: admi70632-sup-0001-SuppMat.pdf.

21967350, 2026, 18, Downloaded from https://advanced.onlinelibrary.wiley.com/doi/10.1002/admi.70632 by Maria Pantano - Universita Di Trento , Wiley Online Library on [13/10/2026]. See the Terms and Conditions (https://onlinelibrary.wiley.com/terms-and-conditions) on Wiley Online Library for rules of use; OA articles are governed by the applicable Creative Commons License